Orbital-selective correlations and renormalized electronic structure in LiFeAs

Huihang Lin,[1] Rong Yu,[1,2,*] Jian-Xin Zhu,[3,†] and Qimiao Si[4,‡]

[1]*Department of Physics and Beijing Key Laboratory of Opto-electronic Functional Materials and Micro-nano Devices, Renmin University of China, Beijing 100872, China*

[2]*Key Laboratory of Quantum State Construction and Manipulation (Ministry of Education), Renmin University of China, Beijing 100872, China*

[3]*Theoretical Division and Center for Integrated Nanotechnologies, Los Alamos National Laboratory, Los Alamos, New Mexico 87545, USA*

[4]*Department of Physics and Astronomy, Rice Center for Quantum Materials, Rice University, Houston, Texas 77005, USA*

(Received 10 March 2021; revised 5 February 2024; accepted 9 February 2024; published 29 February 2024)

Multiorbital physics is important to both the correlation physics and topological behavior of quantum materials. LiFeAs is a prototype iron pnictide suitable for in-depth investigation of this issue. Its electronic structure is strikingly different from the prediction of the noninteracting description. Here, a multiorbital Hubbard model is studied using a $U(1)$ slave-spin theory. We demonstrate a mechanism for a substantial change to the Fermi surface, namely, orbital selectivity of the energy-level renormalization cooperating with its counterpart in quasiparticle spectral weight. Using this effect, we show how the dominating features of the electronic structure in LiFeAs are understood by the local correlations alone. Our results set the stage to understand the origins and nature of both the unconventional superconductivity and likely electronic topology in this prototype iron pnictide and, more generally, reveal a remarkable degree of universality out of the seemingly complex multiorbital building blocks across a broad range of strongly correlated superconductors.

DOI: 10.1103/PhysRevB.109.075170

I. INTRODUCTION

Establishing features that are universal across the different families of strongly correlated systems and identifying properties that are particular to each family are important routes toward elucidating these quantum materials. For iron-based superconductors (FeSCs) [1], an important feature that is of extensive current interest is their multiorbital behavior [2–9]. It has been recognized that electron correlations are strongly orbital dependent in many FeSCs [10–22]. This strong orbital selectivity not only causes large effective mass enhancements [23] and a substantial renormalization of the electronic structure in the normal state [24] but also affects the pairing structure of the superconducting state [25–28]. Previous studies showed that the Hund's rule coupling between the multiple orbitals plays a crucial role in suppressing the interorbital correlations [10,13] and pushes the system toward a novel orbital-selective Mott phase (OSMP), in which the iron d_{xy} orbital is Mott localized while other $3d$ orbitals are still itinerant [12]. In experiments, this OSMP can be accessed from a Fermi-liquid-like metallic phase by increasing the temperature [16]. More recently, angular-resolved photoemission spectroscopy (ARPES) measurements [29] have implicated an OSMP as a ground state in the iron chalcogenides upon isovalent doping [29], and observed a Fermi surface reconstruction associated with the orbital-selective Mott transition (OSMT). The orbital-selective Mott physics is recognized as universal across essentially all the iron chalcogenides [24] and actively interplays with their nematicity and superconductivity [30–34].

In other FeSCs, in particular for iron pnictides, the situation remains open. On general grounds, one may expect that several factors, including the effective orbital dependence in the bandwidth and the extent of the kinetic interorbital hybridization as well as the degree of orbital-degeneracy breaking (crystal level splitting), may interplay with the Hund's coupling and influence the strength of the orbital selectivity. It has been proposed that the orbital selectivity is enhanced when the $3d$ electron occupation number per Fe site is decreased from $n = 6$, the case of the parent compound, toward $n = 5$ [13,35,36]. For the typical iron pnictides with carrier concentrations close to $n = 6$, there is not yet a clear-cut case for orbital-selective correlations.

The 111 iron pnictide LiFeAs presents a promising and pressing case for elucidating the multiorbital correlations of the iron pnictides with broader importance. It superconducts in its pristine form [37,38], and there is no static magnetic or nematic order in its phase diagram. A recent ARPES study [39] reveals features that are reminiscent of the behavior of the iron chalcogenides. In addition, and particularly notably, its correlation-induced renormalization to the electronic structure near the Fermi energy is especially puzzling.

To put the last feature in a larger context, we note that, in general, electron correlations cause mass enhancements, squeezing the bands toward the Fermi level. This is

*rong.yu@ruc.edu.cn
†jxzhu@lanl.gov
‡qmsi@rice.edu

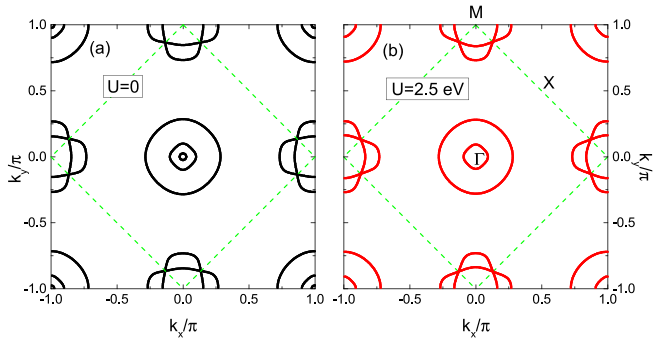

FIG. 1. Shrinkage of the Fermi surface in the model for LiFeAs. The Fermi surfaces are calculated at (a) $U = 0$ and (b) $U = 2.5$ eV. The correlation removes the innermost hole pocket and reduces the other pockets.

captured by a local self-energy which, in single-band/orbital systems, cannot change the Fermi surface from its noninteracting counterpart. Even in multiorbital systems, without orbital selectivity, the Fermi surface would be unchanged given that the mass enhancement factors are identical in all bands. Surprisingly, in some FeSCs, the observed volume of some Fermi pockets is shrunken compared to that from local density approximation (LDA) calculations; this reflects the opposite ("blue/red") correlation-induced shifts of the electron and hole bands [40,41]. In particular for LiFeAs, LDA obtains three hole Fermi pockets centered at the Γ point of the BZ. The outermost one has mainly a d_{xy} orbital character, and the inner two are dominated by the $d_{xz/yz}$ orbitals. By contrast, ARPES measurements show that the band giving the innermost hole pocket in LDA is actually below the Fermi level [42–45]. The origin of the Fermi-pocket reduction is a subject of controversy. In calculations using two-particle self-consistent and/or random phase approximation approaches [46,47], this reduction is attributed to nonlocal electron correlations. A more recent study [48] suggests that the experimental spectrum observed by ARPES can be fitted in terms of a local (i.e., **k**-independent) self-energy.

In this paper, we address the orbital selectivity of LiFeAs, with two findings. First, the small As-Fe-As bond angle helps stabilize an OSMP over a broad parameter regime in the ground-state phase diagram. With increasing temperature, the system is driven through an OSMT. Second, we advance a natural but surprising mechanism for a substantial change in the Fermi surface. We demonstrate an effect, an orbital-selective energy-level renormalization, and show how it cooperates with the orbital dependence in the quasiparticle spectral weight to cause a shrinkage of the Fermi pockets; most drastically, the innermost hole pocket disappears completely (see Fig. 1). Thus, the main features of the electronic structure are captured by the local correlations.

II. MODEL AND METHOD

We study a five-orbital Hubbard model for LiFeAs. The Hamiltonian reads as

$$H = H_{\rm TB} + H_{\rm soc} + H_{\rm int}. \tag{1}$$

$H_{\rm TB}$ is a five-orbital tight-binding Hamiltonian with tetragonal lattice symmetry [49],

$$H_{\rm TB} = \frac{1}{2}\sum_{ij\alpha\beta\sigma} t_{ij}^{\alpha\beta} d_{i\alpha\sigma}^{\dagger} d_{j\beta\sigma} + \sum_{i\alpha\sigma}(\epsilon_\alpha - \mu) d_{i\alpha\sigma}^{\dagger} d_{i\alpha\sigma}, \tag{2}$$

where $d_{i\alpha\sigma}^{\dagger}$ creates an electron in orbital α ($\alpha = 1, \ldots, 5$ denoting xz, yz, $x^2 - y^2$, xy, and $3z^2 - r^2$ orbitals, respectively) with spin σ at site i, ϵ_α refers to the energy level associated with the crystal field splitting (which is diagonal in the orbital basis), and μ is the chemical potential that fixes the total electron density to 6 per Fe. Importantly, the interorbital hopping terms act as a kinetic interorbital hybridization, making the OSMP delicate and different from the conventional treatment [50,51]. The tight-binding parameters $t_{ij}^{\alpha\beta}$ and ϵ_α for LiFeAs are determined by fitting the LDA band structure. The procedure is presented in Appendix A. As shown in Fig. 1(a) [and also, see below, Fig. 5(a)], this model, similar to other tight-binding models [52–54], captures major features of the noninteracting electronic structure of LiFeAs and gives the correct geometry of the LDA Fermi surface. $H_{\rm soc} = \frac{\lambda_{\rm soc}^0}{2}\sum_{i\alpha\beta\sigma\sigma'}(\mathbf{L}\cdot\boldsymbol{\tau})_{\alpha\sigma,\beta\sigma'} d_{i\alpha\sigma}^{\dagger} d_{i\beta\sigma'}$ is an atomic SOC term, where $\mathbf{L}$ denotes the orbital angular momentum operator and $\boldsymbol{\tau}$ refers to the Pauli matrices. We take the bare value of the SOC $\lambda_{\rm soc}^0 = -30$ meV, which is also renormalized in an orbital-selective way. Note that the SOC expands the 5-orbital model to the 10-orbital one defined in the 2-Fe unit cell. The on-site interaction $H_{\rm int}$ reads

$$\begin{aligned} H_{\rm int} = {} & \frac{U}{2}\sum_{i,\alpha,\sigma} n_{i\alpha\sigma} n_{i\alpha\bar{\sigma}} \\ & + \sum_{i,\alpha<\beta,\sigma} \{U' n_{i\alpha\sigma} n_{i\beta\bar{\sigma}} + (U' - J_{\rm H}) n_{i\alpha\sigma} n_{i\beta\sigma} \\ & - J_{\rm H}(d_{i\alpha\sigma}^{\dagger} d_{i\alpha\bar{\sigma}} d_{i\beta\bar{\sigma}}^{\dagger} d_{i\beta\sigma} + d_{i\alpha\sigma}^{\dagger} d_{i\alpha\bar{\sigma}}^{\dagger} d_{i\beta\sigma} d_{i\beta\bar{\sigma}})\}, \end{aligned} \tag{3}$$

where $n_{i\alpha\sigma} = d_{i\alpha\sigma}^{\dagger} d_{i\alpha\sigma}$. Here, U, U', and $J_{\rm H}$ respectively denote the intra- and interorbital repulsion and the Hund's rule coupling, and $U' = U - 2J_{\rm H}$ is taken [55].

We investigate the correlation effects using a $U(1)$ slave-spin theory [50,56], which generalizes the single-band slave-boson theory [57] to multiorbital settings. We express $d_{i\alpha\sigma}^{\dagger} = S_{i\alpha\sigma}^{+} f_{i\alpha\sigma}^{\dagger}$. Here, $S_{i\alpha\sigma}^{+}$ ($f_{i\alpha\sigma}^{\dagger}$) is a quantum $S = 1/2$ spin (fermionic spinon) operator introduced to carry the electron's charge (spin) degree of freedom, and $S_{i\alpha\sigma}^{z} = f_{i\alpha\sigma}^{\dagger} f_{i\alpha\sigma} - \frac{1}{2}$ is a local constraint. At the saddle-point level, the constraint is handled via a Lagrange multiplier λ_α and the slave-spin and spinon operators are decomposed so that λ_α and the quasiparticle spectral weight $Z_\alpha \propto |\langle S_\alpha^{+}\rangle|^2$ are determined self-consistently (see Appendix B for details).

III. ORBITAL SELECTIVITY IN THE GROUND STATE

We first examine the correlation effects of the model by presenting its ground-state phase diagram in Fig. 2(a). It consists of a metallic phase, an OSMP, and a Mott insulator (MI), with increasing the on-site Coulomb repulsion U. In the metallic phase, there is a crossover at $U_{\rm cr}$ (the red dashed line) from a weakly correlated metal (WCM) to a strongly correlated metal (SCM) with strong orbital selectivity, as shown in

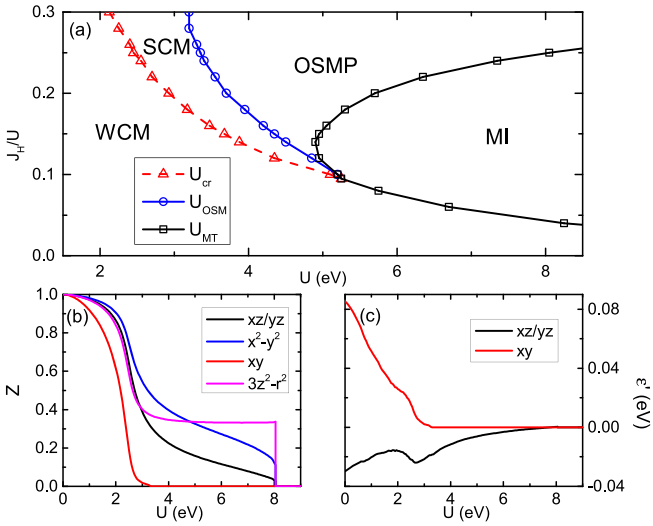

FIG. 2. (a) Ground-state phase diagram of the model for LiFeAs. MI, OSMP, SCM, and WCM denote the Mott insulator phase, orbital-selective Mott phase, and regimes of strongly correlated and weakly correlated metals, respectively. $U_{\rm cr}$ refers to a crossover between WCM and SCM. $U_{\rm OSM}$ and $U_{\rm MT}$ denote the critical U values of the orbital-selective Mott transition and the Mott transition, respectively. (b) Evolution of the orbital-resolved quasiparticle spectral weights Z with U at $J_{\rm H}/U = 0.25$. (c) Effective level energies of the d_{xy} and $d_{xz/yz}$ orbitals vs U at $J_{\rm H}/U = 0.25$.

Fig. 2(b). In the SCM, the system exhibits bad-metal behavior and Z_{xy} is reduced the most. Z_{xy} can be suppressed to zero at $U_{\rm OSM}$, signaling a transition to an OSMP. Further increasing U the system eventually becomes a MI with electrons in all orbitals localized.

The phase diagram of LiFeAs stands out in the iron pnictides. While orbital-selective correlations develop in general, the other parent iron pnictides, such as LaOFeAs, contain no OSMP as a ground state [56]. The stronger orbital selectivity in LiFeAs lies in its smaller As-Fe-As bond angle, which significantly reduces the interorbital hoppings involving the d_{xy} orbital (see Appendix C). Our result represents the first realization in the iron pnictides of an OSMP ground state, which anchors the orbital selectivity in these systems.

IV. TEMPERATURE-INDUCED ORBITAL-SELECTIVE MOTT TRANSITION

Given the proximity to the OSMP in the ground state of LiFeAs, we address whether this OSMP can be approached by increasing the temperature. In Fig. 3(a) we show the evolutions of Z_{xy} and $Z_{xz/yz}$ with temperature at $U = 2.5$ eV and $J_{\rm H}/U = 0.25$. While $Z_{xz/yz}$ shows only a small drop with increasing temperature, Z_{xy} decreases rapidly and vanishes at $T \approx 230$ K, signaling an OSMT. The thermal phase diagram at $J_{\rm H}/U = 0.25$ is presented in Fig. 3(b). The critical U value for the OSMT, $U_{\rm OSM}$, decreases with increasing temperature and merges to the crossover line at $U_{\rm cr}$ at high temperatures. By comparing to the experimental mass enhancement factors [44], we estimate $U \sim 2.4$–2.7 eV for $J_{\rm H}/U = 0.25$ [shaded area in Fig. 3(b)], which results in an OSMT at $T \sim 150$–250 K. This is consistent with the temperature evolution

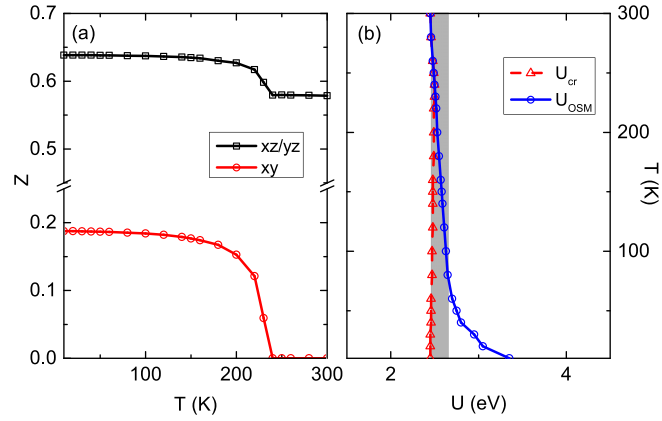

FIG. 3. (a) Evolution of the orbital-resolved quasiparticle spectral weights with temperature at $J_{\rm H}/U = 0.25$ and $U = 2.5$ eV for LiFeAs. An OSMT takes place at about 230 K. (b) The thermal phase diagram of the model for LiFeAs at $J_{\rm H}/U = 0.25$. The shading shows the regime of the estimated U values in LiFeAs.

observed in a recent ARPES experiment [39]. Figure 3(b) and the associated placement in Fig. 2(a) show that LiFeAs is just inside the orbital-selective SCM regime.

V. RENORMALIZATION OF ELECTRONIC STRUCTURE AND SHRINKAGE OF FERMI POCKETS

In a single-orbital model, electron correlations modify the electronic structure by renormalizing the bandwidth while keeping the Fermi surface unchanged as a consequence of the Luttinger theorem. In a multiorbital model with orbital selectivity, with Z being orbital dependent, the situation is considerably richer.

Our key finding is that the renormalization of the energy levels, ϵ_α, is also orbital dependent. This warrants the introduction of a second orbital-selective renormalization factor, Z'_α, for the energy levels:

$$\epsilon'_\alpha = Z'_\alpha \epsilon_\alpha. \tag{4}$$

The renormalized energy level, ϵ'_α, as a function of U is shown in Fig. 2(c). In general, $Z'_\alpha \neq Z_\alpha$ are independent, as illustrated in Fig. 4.

We now show that the orbital-selective energy-level renormalization, Z'_α, can lead to a shrinkage of the Fermi pockets. We start by specifying the orbital dependence of the quasiparticle weight Z, which differentiates the renormalization of the bands with different orbital characters. This is clearly seen in the calculated band structure of LiFeAs in Fig. 5: The bottom of the γ band, with a dominant d_{xy} orbital character, is renormalized from about -0.5 eV to -0.1 eV, with a renormalization factor of about 5, while the bottom of the δ band, with a $d_{xz/yz}$ orbital character, is only renormalized by a factor of about 1.4.

We proceed by focusing on the α, α', and β bands near the Γ point, which mainly have $d_{xz/yz}$ and d_{xy} orbital characters, respectively. Here, the interorbital hybridization can be neglected [58]. The dispersion can then be expressed as

$$E(\mathbf{k}) \approx Z_\alpha \xi_\alpha(\mathbf{k}) + \epsilon'_\alpha = Z_\alpha[\xi_\alpha(\mathbf{k}) + \epsilon_\alpha] + (Z'_\alpha - Z_\alpha)\epsilon_\alpha, \tag{5}$$

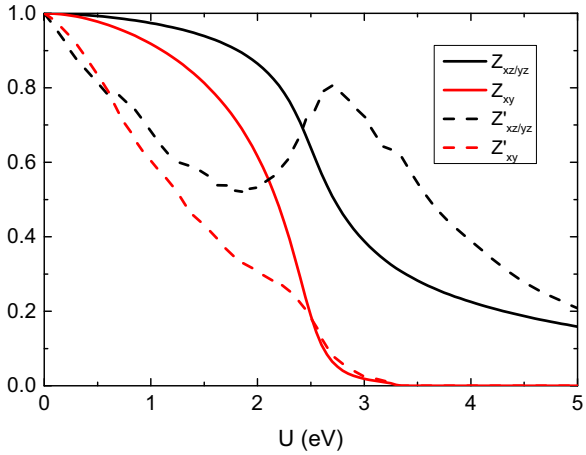

FIG. 4. Evolution of the orbital-resolved quasiparticle spectral weights Z_α and the renormalization factors Z'_α with U at $J_H/U = 0.25$ for LiFeAs.

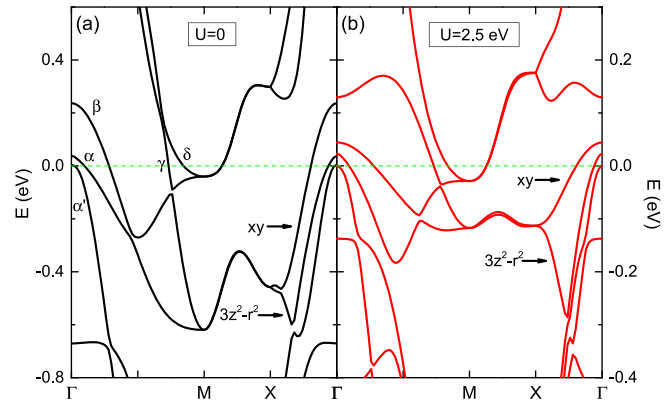

FIG. 5. Comparison of the electronic structures in the model for LiFeAs at (a) $U = 0$ and (b) $U = 2.5$ eV, showing a strong renormalization effect. $J_H/U = 0.25$ and $\lambda^0_{soc} = -30$ meV are taken in the calculation.

where $\xi_\alpha(\mathbf{k})$ is the Fourier component of the hopping parameter $t_{ij}^{\alpha\alpha}$. For simplicity, we have set the Fermi level to $E = 0$, and the Fermi surface in the noninteracting limit is defined by $\xi_\alpha(\mathbf{k}) + \epsilon_\alpha = 0$. Clearly, the Fermi surface is un-renormalized if $Z'_\alpha = Z_\alpha$. Importantly, for $Z'_\alpha \neq Z_\alpha$, the Fermi pocket either shrinks or expands depending on the sign of the last term in Eq. (5). For LiFeAs, taking $J_H/U = 0.25$ and $U = 2.5$ eV, we find from Fig. 2 and Fig. 4 that $Z'_{xy} \approx 0.18 < Z_{xy} \approx 0.19$, $\epsilon_{xy} > 0$, and $Z'_{xz/yz} \approx 0.73 > Z_{xz/yz} \approx 0.63$, $\epsilon_{xz/yz} < 0$. Therefore, according to Eq. (5), the pockets of the α, α', and β sheets are all reduced in size. The difference between Z_{xy} and Z'_{xy} is relatively small, and the Fermi-surface reduction of the β sheet is, correspondingly, relatively small. However, the difference between $Z_{xz/yz}$ and $Z'_{xz/yz}$ is larger, leading to an additional energy-level shift of about 20 meV. This level shift causes a much stronger shrinkage for the inner hole pockets (see Table I for details). Because the innermost α' pocket has the least Fermi wave vector $\mathbf{k}_F$, it is the most susceptible to the level shift. Indeed, it is completely eliminated as shown in Fig. 1 and Fig. 5. Note that the electron pockets also slightly shrink in a way to fulfill the Luttinger theorem.

VI. DISCUSSION AND CONCLUSIONS

Several remarks are in order. First, the calculated low-temperature quasiparticle spectral weights $Z_{xy} \approx 0.2$ and $Z_{xz/yz} \approx 0.6$ in the physical regime agree well with the strong orbital-dependent mass renormalization factors $(m^\star/m_b)_{xy} \sim 4$–5 and $(m^\star/m_b)_{xz/yz} \sim 1.3$–2.3 found in experiments [44]. (We note in passing that the ARPES linewidth in LiFeAs may be influenced by the larger k_z dependence of the xz/yz orbitals than that of the xy orbital [59].) Our results indicate LiFeAs is at the crossover into the strongly orbital-selective regime of the zero-temperature phase diagram, which is confirmed by a recent theoretical work [60]. Relatedly, we show that the system undergoes an OSMT at $T \approx 230$ K, which explains the strong reduction of the xy-orbital spectral weight with increasing temperature as observed in ARPES [39]. Both features are to be contrasted with what happens from the nonlocal correlation effects. The latter would produce a larger renormalization of the quasiparticle weight to the $3d_{xz/yz}$ orbitals than that to the $3d_{xy}$ orbital [46] given that the xz/yz-orbital-hosting inner hole states have a larger phase space than the xy-orbital-hosting outermost hole Fermi pocket for nested coupling to the electron Fermi pockets via the $(\pi, 0)$ interactions; this is opposite to the ARPES observations of LiFeAs. In addition, the nonlocal mechanism does not account for the temperature-induced suppression of the $3d_{xy}$ quasiparticle spectral weight.

Second, and importantly, our work advances a mechanism for the Fermi pocket shrinkage in terms of local, orbital-selective, electron correlations. The key ingredient is our demonstration of the orbital-selective energy-level renormalization Z'_α in Eqs. (4) and (5). The Fermi surface differs from the one in the noninteracting limit only when $Z'_\alpha \neq Z_\alpha$, which is necessarily the case in the presence of orbital selectivity. Our results imply that the dominant effect of electronic structure renormalization in LiFeAs, e.g., the shrinkage of

TABLE I. Areas of the hole pockets without interaction, $A(U = 0)$, and their respective reduction normalized by the corresponding noninteracting area, $\delta A(U) \equiv [A(U = 0) - A(U)]/A(U = 0)$. Here, the areas are shown in units of $(\pi/a)^2$, where a is the nearest-neighbor Fe-Fe distance. The last column shows the estimated hole pocket area reduction in experiments by comparing the ARPES data to the DFT values, which are extracted from Refs. [41,44].

	$A(U = 0)$	$\delta A(U = 2.5$ eV)	$\delta A(U = 2.6$ eV)	$\delta A(U = 2.7$ eV)	$\delta A(U = 2.8$ eV)	δA(exp.)
α' sheet	0.0020	100%	100%	100%	100%	100%
α sheet	0.0278	13%	33%	49%	58%	50%–80%
β sheet	0.2461	2.4%	−4.6%	−9.9%	−13.2%	−10%–10%

inner hole pockets, is understood by the local correlations alone. More generally, our work advances a mechanism for the general phenomenon of "blue/red shifts" [40], namely the differing renormalization of the energy levels and quasiparticle weights, $Z'_\alpha \neq Z_\alpha$. More quantitative aspects of the Fermi surface change are summarized in Table I. It is interesting that a similar effect in ruthenates is seen in *ab initio* calculations [61].

Third, our results suggest that the electronic structure of the iron pnictides, like their iron chalcogenide counterpart, is predominantly influenced by the local electron correlations. Such correlations provide a starting point to understand the nature of the superconducting state [30,31,34]; indeed, our work sets the stage to address the role of short-range interactions in driving the superconductivity of LiFeAs and its derivatives, as has been experimentally implicated [62,63].

We close the discussion by noting several additional features. Because of the strong renormalization of the xy orbital, the $3z^2 - r^2$ band along the Γ-X direction is pushed closer to the Fermi level in LiFeAs, as shown in Fig. 5. This serves as a particularly convenient diagnostic of strong orbital selectivity [29]. In addition, in strongly correlated electronic topology, multiorbital correlations can play a crucial role for the band inversion and other inherent multiband behavior. LiFeAs is emerging as a candidate system in which its band topology in the bulk leads to topologically nontrivial superconductivity on its surface [64]. Given the important role that strong correlations are expected to play in the band inversion of Fe-based systems [65], the orbital-selective correlations we have advanced for LiFeAs set the stage for the much-needed understanding of the topological behavior in LiFeAs. In this connection, we note that, taking into account the renormalization effect on the SOC, the calculated splitting between the α and α' bands is about 20 meV [Fig. 5(b)], which is consistent with the reported value in experiments [42,45].

Our results suggest that the electronic structure of the iron pnictides, like their iron chalcogenide counterpart, is strongly influenced by the local electron correlations. Such correlations underlie the bad-metal normal state observed in many families of strongly correlate superconductors. Our results not only provide the understanding of a striking puzzle in the iron pnictides but also uncover a hidden simplicity in the seeming complexity of the multiorbital superconductors. This implicates a remarkable degree of universality across the iron-based superconductors that is shared with many other families of strongly correlated superconductors.

Note added. Recently, we became aware that the behavior we predicted in Fig. 3(b) has been experimentally observed [66].

ACKNOWLEDGMENTS

We thank M. Yi. J. W. Huang, A. Damascelli, R. Day, and P. C. Dai for useful discussions. Work at Renmin University of China has been supported by the National Key R&D Program of China, Grant No. 2023YFA1406500, and the National Science Foundation of China, Grants No. 12334008 and No. 12174441 (R.Y.), and by the Fundamental Research Funds for the Central Universities, and the Research Funds of Renmin University of China, Grant No. 22XNH096 (H.L.). Work at Rice University has been supported by the U.S. Department of Energy, Office of Science, Basic Energy Sciences, under Award No. DE-SC0018197, and the Robert A. Welch Foundation, Grant No. C-1411 (Q.S.). Work at Los Alamos was carried out under the auspices of the U.S. DOE NNSA under Contract No. 89233218CNA000001. It was supported by the LANL LDRD program and in part by the Center for Integrated Nanotechnologies, a U.S. DOE BES user facility. Q.S. acknowledges the hospitality of the Aspen Center for Physics, which is supported by NSF Grant No. PHY-2210452.

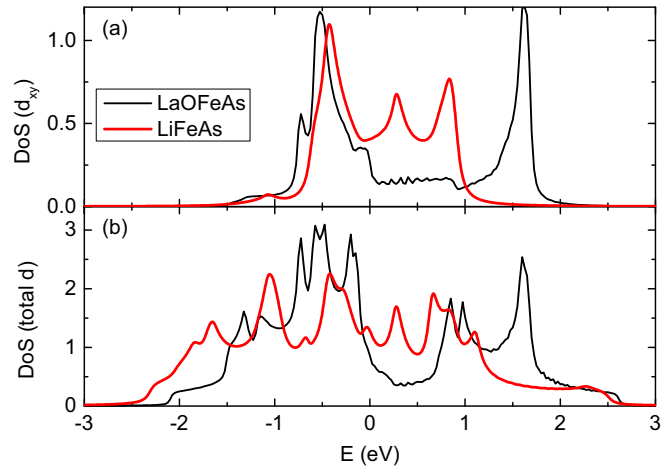

FIG. 6. Density of states (DoS) projected onto the d_{xy} [in (a)] and the total d orbitals [in (b)] at $U = 0$ of models for LiFeAs (red curves) and LaOFeAs (black curves), respectively.

APPENDIX A: DETAILS ON THE TIGHT-BINDING MODEL

To include the realistic band structure at low energies into our tight-binding modeling, we have first carried out band structure calculations for LiFeAs (space group: $P4/nmm$) within the framework of density functional theory (DFT). We have used the full-potential linearized augmented plane wave (FP-LAPW) method as implemented in the WIEN2k code [67]. The generalized gradient approximation was chosen for the exchange-correlation functional. Experimental lattice parameters ($a = b = 3.776360$ Å, $c = 6.35679$ Å) [68] were used in the simulations. We then follow the procedure suggested by Graser *et al.* [69] to fit the Wannierized bands [70,71] with a five-orbital tight-banding Hamiltonian [49], unfolding the small two Fe per unit cell BZ to a large one Fe per unit cell BZ. In this procedure, an interface [72] between the WIEN2k code and the wannier90 code [73] is also employed. The tight-binding parameters so derived are listed in Table II.

The electronic structure of the tight-binding model is shown in Fig. 5(a), which produces the Fermi surface of three hole pockets centered about the Γ point and two electron pockets centered about the M point, as presented in Fig. 1(a).

To clarify the origin of the enhanced orbital selectivity compared to other parent iron pnictides, we calculated the total density of states (DoS) and the DoS projected to the d_{xy} of the tight-binding model. They are contrasted to those of the tight-binding model for LaOFeAs [49] in Fig. 6. Though the overall DoS of the two models are comparable, the DoS

TABLE II. Tight-binding parameters of the five-orbital model for LiFeAs. Here we use the same notation as in Ref. [49]. The orbital index $\alpha = 1, 2, 3, 4, 5$ corresponds to d_{xz}, d_{yz}, $d_{x^2-y^2}$, d_{xy}, and $d_{3z^2-r^2}$ orbitals, respectively. The listed parameters are in eV.

	$\alpha=1$	$\alpha=2$	$\alpha=3$	$\alpha=4$	$\alpha=5$		
ϵ_α	0.06517	0.06517	−0.38097	0.18026	−0.63628		
$t_\mu^{\alpha\alpha}$	$\mu=x$	$\mu=y$	$\mu=xy$	$\mu=xx$	$\mu=xxy$	$\mu=xyy$	$\mu=xxyy$
$\alpha=1$	−0.02507	−0.49888	0.24903	0.04834	0.00813	−0.02776	0.04531
$\alpha=3$	0.42894		−0.01946	−0.01032			
$\alpha=4$	0.16275		0.13559	−0.00441	−0.05245		−0.03593
$\alpha=5$	−0.08510			−0.04632	0.01048		−0.00195
$t_\mu^{\alpha\beta}$	$\mu=x$	$\mu=xy$	$\mu=xxy$	$\mu=xxyy$			
$\alpha\beta=12$		0.19318	−0.05864	0.07046			
$\alpha\beta=13$	−0.42376	0.07714	0.01353				
$\alpha\beta=14$	0.03406	−0.02355	−0.00376				
$\alpha\beta=15$	−0.14608	−0.09700		−0.00683			
$\alpha\beta=34$			−0.00635				
$\alpha\beta=35$	−0.26547		0.03472				
$\alpha\beta=45$		−0.10611		0.03363			

projected to the d_{xy} orbital in the model of LiFeAs has a much narrower bandwidth (∼2 eV) than in LaOFeAs (∼3 eV). This indeed suggests a stronger orbital selectivity in LiFeAs; see the main text for a detailed discussion.

APPENDIX B: DETAILS ON THE $U(1)$ SLAVE-SPIN THEORY

Here we present a brief introduction to the $U(1)$ slave-spin method. For more details, we refer to Refs. [50,56].

In the $U(1)$ slave-spin formulation, we introduce a quantum $S = 1/2$ spin operator whose XY component ($S^+_{i\alpha\sigma}$) is used to represent the charge degree of freedom of the electron at each site i, in each orbital α, and for each spin flavor σ. Correspondingly, we introduce a fermionic "spinon" operator ($f^\dagger_{i\alpha\sigma}$) to carry the spin degree of freedom. The electron creation operator is represented as follows,

$$d^\dagger_{i\alpha\sigma} = S^+_{i\alpha\sigma} f^\dagger_{i\alpha\sigma}. \tag{B1}$$

This representation has an enlarged Hilbert space compared to the one for the physical d electrons. To restrict the Hilbert space to the physical one, we implement a local constraint,

$$S^z_{i\alpha\sigma} = f^\dagger_{i\alpha\sigma} f_{i\alpha\sigma} - \tfrac{1}{2}. \tag{B2}$$

This representation contains a $U(1)$ gauge redundancy corresponding to $f^\dagger_{i\alpha\sigma} \to f^\dagger_{i\alpha\sigma} e^{-i\theta_{i\alpha\sigma}}$ and $S^+_{i\alpha\sigma} \to S^+_{i\alpha\sigma} e^{i\theta_{i\alpha\sigma}}$. As a result, the slave spins can be used to carry the $U(1)$-symmetric physical charge degree of freedom, similarly as in the slave-rotor approach [74].

To ensure that the saddle point captures the correct quasiparticle spectral weight in the noninteracting limit (being equal to 1), we define a dressed operator in the Schwinger boson representation of the slave spins (in a way similar to the standard slave-boson theory [57]):

$$\hat{z}^\dagger_{i\alpha\sigma} = P^+_{i\alpha\sigma} S^+_{i\alpha\sigma} P^-_{i\alpha\sigma}, \tag{B3}$$

where $P^\pm_{i\alpha\sigma} = 1/\sqrt{1/2 + \delta \pm S^z_{i\alpha\sigma}}$, and δ is an infinitesimal positive number to regulate $P^\pm_{i\alpha\sigma}$. With this construction, Eq. (B1) becomes

$$d^\dagger_{i\alpha\sigma} = \hat{z}^\dagger_{i\alpha\sigma} f^\dagger_{i\alpha\sigma}. \tag{B4}$$

The Hamiltonian given in Eq. (1) of the main text can then be effectively rewritten as

$$H = \frac{1}{2}\sum_{ij\alpha\beta\sigma} t^{\alpha\beta}_{ij} \hat{z}^\dagger_{i\alpha\sigma} \hat{z}_{j\beta\sigma} f^\dagger_{i\alpha\sigma} f_{j\beta\sigma} + \sum_{i\alpha\sigma} (\epsilon_\alpha - \mu) f^\dagger_{i\alpha\sigma} f_{i\alpha\sigma} - \lambda_{i\alpha\sigma}[f^\dagger_{i\alpha\sigma} f_{i\alpha\sigma} - S^z_{i\alpha\sigma} - 1/2] + H^S_{\rm int}.$$

Here, $\lambda_{i\alpha\sigma}$ is a Lagrange multiplier used to enforce the constraint in Eq. (B2). In addition, $H^S_{\rm int}$ is the interaction Hamiltonian in Eq. (3) of the main text rewritten in the slave-spin representation $H_{\rm int} \to H_{\rm int}(\mathbf{S})$ [56]. The quasiparticle spectral weight

$$Z_{i\alpha\sigma} = |\langle \hat{z}_{i\alpha\sigma} \rangle|^2 \propto |\langle S^+_{i\alpha\sigma} \rangle|^2. \tag{B5}$$

After decomposing the slave-spin and spinon operators and treating the constraint on average, we obtain two saddle-point Hamiltonians for the spinons and the slave spins, respectively:

$$H^{\rm mf}_f = \sum_{k\alpha\beta} \left[\xi^{\alpha\beta}_k \langle \tilde{z}^\dagger_\alpha \rangle \langle \tilde{z}_\beta \rangle + \delta_{\alpha\beta}(\epsilon_\alpha - \lambda_\alpha - \mu)\right] f^\dagger_{k\alpha} f_{k\beta}, \tag{B6}$$

$$H^{\rm mf}_S = \sum_{\alpha\beta} \left[Q^f_{\alpha\beta}(\langle \tilde{z}^\dagger_\alpha \rangle \tilde{z}_\beta + \langle \tilde{z}_\beta \rangle \tilde{z}^\dagger_\alpha) + \delta_{\alpha\beta}(\lambda_\alpha - \tilde{\mu}_\alpha) S^z_\alpha\right] + H^S_{\rm int}, \tag{B7}$$

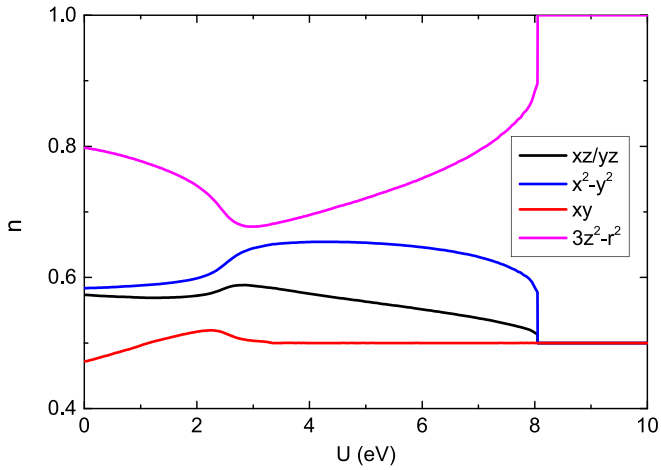

FIG. 7. Evolution of the orbital-resolved electron occupation number n with U at $J_H/U = 0.25$ for LiFeAs.

where $\delta_{\alpha\beta}$ is Kronecker's delta function, $\xi_k^{\alpha\beta} = \frac{1}{N}\sum_{ij\sigma} t_{ij}^{\alpha\beta} e^{ik(r_i - r_j)}$, and

$$Q_{\alpha\beta}^f = \sum_{k\sigma} \xi_k^{\alpha\beta} \langle f_{k\alpha\sigma}^\dagger f_{k\beta\sigma}\rangle/2. \tag{B8}$$

In addition, $\tilde{\mu}_\alpha$ is an effective on-site potential whose definition is given in Ref. [56].

Equations (B6) and (B7) represent the main formulation of the $U(1)$ slave-spin approach at the saddle-point level. We study the metal-to-insulator transitions in the paramagnetic phase preserving the translational symmetry. The latter allows us to drop the spin and/or site indices of the slave spins and the Lagrange multiplier λ_α in Eqs. (B6) and (B7). We refer to Refs. [50,56] for a detailed derivation of these saddle-point Hamiltonians. At the saddle-point level, Z_α and λ_α are solved self-consistently. In the single-band Hubbard model, the slave-spin method is reduced to the standard slave-boson method [57]. At half filling, it gives rise to a quasiparticle weight Z going to zero when U approaches to a finite value U_c, where the transition to the Mott insulator takes place, in a linear fashion: $Z \sim (U_c - U)$. This result is consistent with the well-established Brinkman-Rice result [75] as derived from, e.g., the Gutzwiller wave function method. For a general multiorbital model three saddle-point solutions can be stabilized: a metallic state with the quasiparticle spectral weight $Z_\alpha > 0$ in all the orbitals, a Mott insulator (MI) with $Z_\alpha = 0$ in all the orbitals with a gapless spinon spectrum, and an OSMP in which $Z_\alpha = 0$ in some orbitals whereas $Z_\alpha > 0$ in the others. The solution of the model for LiFeAs is presented in Fig. 2, along with Fig. 7.

In this work, we focus on the electronic band structure in the metallic phase. In this phase, the quasiparticle spectral weights are nonzero in all orbitals, and the $U(1)$ gauge fields are gapped (the corresponding gauge theory is in the Higgs phase) and will be irrelevant to the low-energy physics near the Fermi level. At the saddle-point level, the spinon dispersion is identical to the one of the physical electrons in the metallic phase, with both being naturally renormalized by the quasiparticle spectral weights $\sqrt{Z_\alpha Z_\beta}$ and shifted by the effective level energy $\epsilon'_\alpha = \epsilon_\alpha - \lambda_\alpha = Z'_\alpha \epsilon_\alpha$, where Z'_α is a function of Z_α and λ_α of all the orbitals. (Here we set the Fermi level at zero energy.)

We now turn to the effect of the spin-orbit coupling (SOC). In the models for iron-based superconductors, the spin-orbit coupling $\lambda_{\rm soc}^0$ is about 10–30 meV, which is much smaller than the bandwidth of the Fe $3d$ electrons or the dominant interactions (either is of several eVs). For this reason, the SOC will have a negligible effect as far as the quasiparticle spectral weights (Z's) are concerned. We thus adopt the following strategy: (1) performing the self-consistent slave-spin calculation (as described above) without the SOC term to obtain the Z values; (2) adding the SOC as a perturbation in an effective tight-binding model with the obtained renormalization factors (Z's). For example, the spinon dispersion is determined by the following model:

$$H_f^{\rm mf,SOC} = H_f^{\rm mf} + \frac{\lambda_{\rm soc}^0}{2} \sum_{i\alpha\beta\sigma\sigma'} (\tilde{\mathbf{L}}\cdot\boldsymbol{\tau})_{\alpha\sigma,\beta\sigma'} f_{i\alpha\sigma}^\dagger f_{i\beta\sigma'}, \tag{B9}$$

where $\tilde{\mathbf{L}}_{\alpha\beta} = \sqrt{Z_\alpha Z_\beta}\mathbf{L}_{\alpha\beta}$ is the renormalized orbital angular momentum.

APPENDIX C: BOND ANGLE AND ENHANCED ORBITAL SELECTIVITY IN LiFeAs

As shown in Fig. 2(a) of the main text, the ground-state phase diagram of LiFeAs contains a large regime of OSMP. This differs qualitatively from other parent iron pnictides for which the OSMP was not stabilized in the ground state [56]; it shows that, in the overall phase diagram of the iron pnictides, the OSMP anchors the SCM phase with a large orbital selectivity. To understand this enhanced orbital selectivity in LiFeAs, we note that its As-Fe-As bond angle is about 103°, which is much smaller than those of other parent iron pnictides ($\gtrsim$110°), but is similar to that in $Li_{0.8}Fe_{0.2}OHFeSe$ [9,68]. A smaller bond angle corresponds to an elongated tetragon that significantly reduces the interorbital hoppings involving the d_{xy} orbital because of the in-plane symmetry of this orbital. This is clearly seen by comparing the interorbital hoppings of LiFeAs in Table II to those of LaOFeAs in Ref. [49]. Smaller interorbital hoppings result in narrower bandwidth projected to the d_{xy} orbital. As shown in Fig. 6, the projected band of the d_{xy} orbital in LiFeAs is much narrower than that of LaOFeAs though the overall d-orbital bandwidths are comparable between the two cases. This feature leads to the stronger orbital selectivity in LiFeAs.

[1] Y. Kamihara, T. Watanabe, M. Hirano, and H. Hosono, Iron-based layered superconductor La[$O_{1-x}F_x$]FeAs (x = 0.05–0.12) with T_c = 26 K, J. Am. Chem. Soc. **130**, 3296 (2008).

[2] D. C. Johnston, The puzzle of high temperature superconductivity in layered iron pnictides and chalcogenides, Adv. Phys. **59**, 803 (2010).

[3] F. Wang and D.-H. Lee, The electron-pairing mechanism of iron-based superconductors, Science **332**, 200 (2011).

[4] E. Dagotto, *Colloquium:* The unexpected properties of alkali metal iron selenide superconductors, Rev. Mod. Phys. **85**, 849 (2013).

[5] P. Dai, Antiferromagnetic order and spin dynamics in iron-based superconductors, Rev. Mod. Phys. **87**, 855 (2015).

[6] Q. Si, R. Yu, and E. Abrahams, High temperature superconductivity in iron pnictides and chalcogenides, Nat. Rev. Mater. **1**, 16017 (2016).

[7] P. J. Hirschfeld, Using gap symmetry and structure to reveal the pairing mechanism in Fe-based superconductors, C. R. Phys. **17**, 197 (2016).

[8] E. Bascones, B. Valenzuela, and M. J. Calderón, Magnetic interactions in iron superconductors: A review, C. R. Phys. **17**, 36 (2016).

[9] M. Yi, Y. Zhang, Z.-X. Shen, and D.-H. Lu, Role of the orbital degree of freedom in iron-based superconductors, npj Quantum Mater. **2**, 57 (2017).

[10] R. Yu and Q. Si, Mott transition in multiorbital models for iron pnictides, Phys. Rev. B **84**, 235115 (2011).

[11] Z. P. Yin, K. Haule, and G. Kotliar, Magnetism and charge dynamics in iron pnictides, Nat. Phys. **7**, 294 (2011).

[12] R. Yu and Q. Si, Orbital-selective Mott phase in multiorbital models for alkaline iron selenides $K_{1-x}Fe_{2-y}Se_2$, Phys. Rev. Lett. **110**, 146402 (2013).

[13] L. de' Medici, G. Giovannetti, and M. Capone, Selective Mott physics as a key to iron superconductors, Phys. Rev. Lett. **112**, 177001 (2014).

[14] S. Backes, H. O. Jeschke, and R. Valenti, Microscopic nature of correlations in multiorbital AFe_2As_2 (A = K, Rb, Cs): Hund's coupling versus Coulomb repulsion, Phys. Rev. B **92**, 195128 (2015).

[15] N. Patel, A. Nocera, G. Alvarez, A. Moreo, S. Johnston, and E. Dagotto, Fingerprints of an orbital-selective Mott phase in the block magnetic state of $BaFe_2Se_3$ ladders, Commun. Phys. **2**, 64 (2019).

[16] M. Yi, D. H. Lu, R. Yu, S. C. Riggs, J.-H. Chu, B. Lv, Z. K. Liu, M. Lu, Y. T. Cui, M. Hashimoto, S.-K. Mo, Z. Hussain, C. W. Chu, I. R. Fisher, Q. Si, and Z.-X. Shen, Observation of temperature-induced crossover to an orbital-selective Mott phase in $A_xFe_{2-y}Se_2$ (A = K, Rb) superconductors, Phys. Rev. Lett. **110**, 067003 (2013).

[17] Z. Wang, M. Schmidt, J. Fischer, V. Tsurkan, M. Greger, D. Vollhardt, A. Loidl, and J. Deisenhofer, Orbital-selective metal-insulator transition and gap formation above T_c in superconducting $Rb_{1-x}Fe_{2-y}Se_2$, Nat. Commun. **5**, 3202 (2014).

[18] X. Ding, Y. Pan, H. Yang, and H.-H. Wen, Strong and nonmonotonic temperature dependence of Hall coefficient in superconducting $K_xFe_{2-y}Se_2$ single crystals, Phys. Rev. B **89**, 224515 (2014).

[19] M. Wang, M. Yi, H. Cao, C. de la Cruz, S. K. Mo, Q. Z. Huang, E. Bourret-Courchesne, P. Dai, D. H. Lee, Z. X. Shen, and R. J. Birgeneau, Mott localization in a pure stripe antiferromagnet $Rb_{1-\delta}Fe_{1.5-\sigma}S_2$, Phys. Rev. B **92**, 121101(R) (2015).

[20] X. H. Niu, S. D. Chen, J. Jiang, Z. R. Ye, T. L. Yu, D. F. Xu, M. Xu, Y. Feng, Y. J. Yan, B. P. Xie, J. Zhao, D. C. Gu, L. L. Sun, Q. Mao, H. Wang, M. Fang, C. J. Zhang, J. P. Hu, Z. Sun, and D. L. Feng, A unifying phase diagram with correlation-driven superconductor-to-insulator transition for the 122* series of iron chalcogenides, Phys. Rev. B **93**, 054516 (2016).

[21] M. Hiraishi, K. M. Kojima, H. Okabe, S. Takeshita, A. Koda, R. Kadono, R. Khasanov, S. Iimura, S. Matsuishi, and H. Hosono, Magnetism driven by strong electronic correlation in the heavily carrier-doped iron oxypnictide $LaFeAsO_{0.49}H_{0.51}$, Phys. Rev. B **101**, 174414 (2020).

[22] J. Si, G.-Y. Chen, Q. Li, X. Zhu, H. Yang, and H.-H. Wen, Unconventional superconductivity induced by suppressing an iron-selenium-based Mott insulator $CsFe_{4-x}Se_4$, Phys. Rev. X **10**, 041008 (2020).

[23] Z.-K. Liu, M. Yi, Y. Zhang, J. Hu, R. Yu, J.-X. Zhu, R.-H. He, Y. L. Chen, M. Hashimoto, R. G. Moore, S.-K. Mo, Z. Hussain, Q. Si, Z. Q. Mao, D. H. Lu, and Z.-X. Shen, Experimental observation of incoherent-coherent crossover and orbital-dependent band renormalization in iron chalcogenide superconductors, Phys. Rev. B **92**, 235138 (2015).

[24] M. Yi, Z.-K. Liu, Y. Zhang, R. Yu, J.-X. Zhu, J. J. Lee, R. G. Moore, F. T. Schmitt, W. Li, S. C. Riggs, J.-H. Chu, B. Lv, J. Hu, T. J. Liu, M. Hashimoto, S.-K. Mo, Z. Hussain, Z. Q. Mao, C. W. Chu, I. R. Fisher *et al.*, Observation of universal strong orbital-dependent correlation effects in iron chalcogenides, Nat. Commun. **6**, 7777 (2015).

[25] R. Yu, J.-X. Zhu, and Q. Si, Orbital-selective superconductivity, gap anisotropy, and spin resonance excitations in a multiorbital t-J_1-J_2 model for iron pnictides, Phys. Rev. B **89**, 024509 (2014).

[26] Z. P. Yin, K. Haule, and G. Kotliar, Spin dynamics and orbital-antiphase pairing symmetry in iron-based superconductors, Nat. Phys. **10**, 845 (2014).

[27] T. Ong, P. Coleman, and J. Schmalian, Concealed d-wave pairs in the $s^{\pm}$ condensate of iron-based superconductors, Proc. Natl. Acad. Sci. USA **113**, 5486 (2016).

[28] E. M. Nica, R. Yu, and Q. Si, Orbital selective pairing and superconductivity in iron selenides, npj Quantum Mater. **2**, 24 (2017).

[29] J. Huang, R. Yu, Z. Xu, J.-X. Zhu, J. S. Oh, Q. Jiang, M. Wang, H. Wu, T. Chen, J. D. Denlinger, S.-K. Mo, M. Hashimoto, M. Michiardi, T. M. Pedersen, S. Gorovikov, S. Zhdanovich, A. Damascelli, G. Gu, P. Dai, J.-H. Chu *et al.*, Correlation-driven electronic reconstruction in $FeTe_{1-x}Se_x$, Commun. Phys. **5**, 29 (2022).

[30] P. O. Sprau, A. Kostin, A. Kreisel, A. E. Böhmer, V. Taufour, P. C. Canfield, S. Mukherjee, P. J. Hirschfeld, B. M. Andersen, and J. C. Séamus Davis, Discovery of orbital-selective Cooper pairing in FeSe, Science **357**, 75 (2017).

[31] A. Kostin, P. O. Sprau, A. Kreisel, Yi Xue Chong, A. E. Böhmer, P. C. Canfield, P. J. Hirschfeld, B. M. Andersen, and J. C. Séamus Davis, Imaging orbital-selective quasiparticles in the Hund's metal state of FeSe, Nat. Mater. **17**, 869 (2018).

[32] L. Fanfarillo, G. Giovannetti, M. Capone, and E. Bascones, Nematicity at the Hund's metal crossover in iron superconductors, Phys. Rev. B **95**, 144511 (2017).

[33] R. Yu, J.-X. Zhu, and Q. Si, Orbital selectivity enhanced by nematic order in FeSe, Phys. Rev. Lett. **121**, 227003 (2018).

[34] H. Hu, R. Yu, E. M. Nica, J.-X. Zhu, and Q. Si, Orbital-selective superconductivity in the nematic phase of FeSe, Phys. Rev. B **98**, 220503(R) (2018).

[35] R. Yu, J.-X. Zhu, and Q. Si, Orbital-dependent effects of electron correlations in microscopic models for iron-based

superconductors, Curr. Opin. Solid State Mater. Sci. **17**, 65 (2013).
[36] F. Eilers, K. Grube, D. A. Zocco, T. Wolf, M. Merz, P. Schweiss, R. Heid, R. Eder, R. Yu, J.-X. Zhu, Q. Si, T. Shibauchi, and H. Löhneysen, Quantum criticality in $A\mathrm{Fe}_2\mathrm{As}_2$ with A = K, Rb, and Cs, Phys. Rev. Lett. **116**, 237003 (2016).
[37] X. C. Wang, Q. Q. Liu, Y. X. Lv, W. B. Gao, L. X. Yang, R. C. Yu, F. Y. Li, and C. Q. Jin, The superconductivity at 18 K in LiFeAs system, Solid State Commun. **148**, 538 (2008).
[38] J. H. Tapp, Z. Tang, B. Lv, K. Sasmal, B. Lorenz, P. C. W. Chu, and A. M. Guloy, LiFeAs: An intrinsic FeAs-based superconductor with T_c = 18 K, Phys. Rev. B **78**, 060505(R) (2008).
[39] H. Miao, Z. P. Yin, S. F. Wu, J. M. Li, J. Ma, B.-Q. Lv, X. P. Wang, T. Qian, P. Richard, L.-Y. Xing, X.-C. Wang, C. Q. Jin, K. Haule, G. Kotliar, and H. Ding, Orbital-differentiated coherence-incoherence crossover identified by photoemission spectroscopy in LiFeAs, Phys. Rev. B **94**, 201109(R) (2016).
[40] L. Ortenzi, E. Cappelluti, L. Benfatto, and L. Pietronero, Fermi-surface shrinking and interband coupling in iron-based pnictides, Phys. Rev. Lett. **103**, 046404 (2009).
[41] G. Lee, H. S. Ji, Y. Kim, C. Kim, K. Haule, G. Kotliar, B. Lee, S. Khim, K. H. Kim, K. S. Kim, K.-S. Kim, and J. H. Shim, Orbital selective Fermi surface shifts and mechanism of high T_c superconductivity in correlated AFeAs (A = Li, Na), Phys. Rev. Lett. **109**, 177001 (2012).
[42] S. V. Borisenko, D. V. Evtushinsky, Z.-H. Liu, I. Morozov, R. Kappenberger, S. Wurmehl, B. Büchner, A. N. Yaresko, T. K. Kim, M. Hoesch, T. Wolf and N. D. Zhigadlo, Direct observation of spin-orbit coupling in iron-based superconductors, Nat. Phys. **12**, 311 (2016).
[43] V. Brouet, D. LeBoeuf, P.-H. Lin, J. Mansart, A. Taleb-Ibrahimi, P. Le Fèvre, F. Bertran, A. Forget, and D. Colson, ARPES view of orbitally resolved quasiparticle lifetimes in iron pnictides, Phys. Rev. B **93**, 085137 (2016).
[44] J. Fink, J. Nayak, E. D. L. Rienks, J. Bannies, S. Wurmehl, S. Aswartham, I. Morozov, R. Kappenberger, M. A. ElGhazali, L. Craco, H. Rosner, C. Felser, and B. Büchner, Evidence of hot and cold spots on the Fermi surface of LiFeAs, Phys. Rev. B **99**, 245156 (2019).
[45] R. P. Day, G. Levy, M. Michiardi, B. Zwartsenberg, M. Zonno, F. Ji, E. Razzoli, F. Boschini, S. Chi, R. Liang, P. K. Das, I. Vobornik, J. Fujii, W. N. Hardy, D. A. Bonn, I. S. Elfimov, and A. Damascelli, Influence of spin-orbit coupling in iron-based superconductors, Phys. Rev. Lett. **121**, 076401 (2018).
[46] K. Zantout, S. Backes, and R. Valentí, Effect of nonlocal correlations on the electronic structure of LiFeAs, Phys. Rev. Lett. **123**, 256401 (2019).
[47] S. Bhattacharyya, K. Björnson, K. Zantout, D. Steffensen, L. Fanfarillo, A. Kreisel, R. Valentí, B. M. Andersen, and P. J. Hirschfeld, Non-local correlations in iron pnictides and chalcogenides, Phys. Rev. B **102**, 035109 (2020).
[48] M. Kim, H. Miao, S. Choi, M. Zingl, A. Georges, and G. Kotliar, On the spatial locality of electronic correlations in LiFeAs, Phys. Rev. B **103**, 155107 (2021).
[49] S. Graser, T. A. Maier, P. J. Hirschfeld, and D. J. Scalapino, Near-degeneracy of several pairing channels in multiorbital models for the Fe pnictides, New J. Phys. **11**, 025016 (2009).
[50] R. Yu and Q. Si, Orbital-selective Mott phase in multiorbital models for iron pnictides and chalcogenides, Phys. Rev. B **96**, 125110 (2017).
[51] Y. Komijani and G. Kotliar, Analytical slave-spin mean-field approach to orbital selective Mott insulators, Phys. Rev. B **96**, 125111 (2017).
[52] H. Eschrig and K. Koepernik, Tight-binding models for the iron-based superconductors, Phys. Rev. B **80**, 104503 (2009).
[53] T. Miyake, K. Nakamura, R. Arita, and M. Imada, Comparison of *ab initio* low-energy models for LaFePO, LaFeAsO, $\mathrm{BaFe}_2\mathrm{As}_2$, LiFeAs, FeSe, and FeTe: Electron correlation and covalency, J. Phys. Soc. Jpn. **79**, 044705 (2010).
[54] M. N. Gastiasoro, P. J. Hirschfeld, and B. M. Andersen, Impurity states and cooperative magnetic order in Fe-based superconductors, Phys. Rev. B **88**, 220509(R) (2013).
[55] C. Castellani, C. R. Natoli, and J. Ranninger, Magnetic structure of V_2O_3 in the insulating phase, Phys. Rev. B **18**, 4945 (1978).
[56] R. Yu and Q. Si, $U(1)$ slave-spin theory and its application to Mott transition in a multiorbital model for iron pnictides, Phys. Rev. B **86**, 085104 (2012).
[57] G. Kotliar and A. E. Ruckenstein, New functional integral approach to strongly correlated Fermi systems: The Gutzwiller approximation as a saddle point, Phys. Rev. Lett. **57**, 1362 (1986).
[58] This refers to the nondegenerate orbitals. In the subspace of the degenerate d_{xz} and d_{yz} orbitals, which share the same mass renormalization factor, moving from the orbital to the band basis does not affect the discussion below.
[59] R. P. Day and A. Damascelli (private communication).
[60] P. Villar Arribi and L. de'Medici, Hund's metal crossover and superconductivity in the 111 family of iron-based superconductors, Phys. Rev. B **104**, 125130 (2021).
[61] G. Zhang, E. Gorelov, E. Sarvestani, and E. Pavarini, Fermi surface of $\mathrm{Sr}_2\mathrm{RuO}_4$: Spin-orbit and anisotropic Coulomb interaction effects, Phys. Rev. Lett. **116**, 106402 (2016).
[62] H. Miao, T. Qian, X. Shi, P. Richard, T. K. Kim, M. Hoesch, L. Y. Xing, X.-C. Wang, C.-Q. Jin, J.-P. Hu, and H. Ding, Observation of strong electron pairing on bands without Fermi surfaces in $\mathrm{LiFe}_{1-x}\mathrm{Co}_x\mathrm{As}$, Nat. Commun. **6**, 6056 (2015).
[63] K. Umezawa, Y. Li, H. Miao, K. Nakayama, Z.-H. Liu, P. Richard, T. Sato, J. B. He, D.-M. Wang, G. F. Chen, H. Ding, T. Takahashi, and S.-C. Wang, Unconventional anisotropic s-wave superconducting gaps of the LiFeAs iron-pnictide superconductor, Phys. Rev. Lett. **108**, 037002 (2012).
[64] P. Zhang, Z. Wang, X. Wu, K. Yaji, Y. Ishida, Y. Kohama, G. Dai, Y. Sun, C. Bareille, K. Kuroda, T. Kondo, K. Okazaki, K. Kindo, X. Wang, C. Jin, J. Hu, R. Thomale, K. Sumida, S. Wu, K. Miyamoto *et al.*, Multiple topological states in iron-based superconductors, Nat. Phys. **15**, 41 (2019).
[65] H. Lohani, T. Hazra, A. Ribak, Y. Nitzav, H. Fu, B. Yan, M. Randeria, and A. Kanigel, Band inversion and topology of the bulk electronic structure in $\mathrm{FeSe}_{0.45}\mathrm{Te}_{0.55}$, Phys. Rev. B **101**, 245146 (2020).
[66] Y. Cai, J. Huang *et al.* (unpublished).
[67] P. Blaha *et al.*, *An Augmented Plane Wave + Local Orbitals Program for Calculating Crystal Properties* (K. Schwarz, Tech. Universität Wien, Austria, 2001).
[68] M. J. Pitcher, D. R. Parker, P. Adamson, S. J. C. Herkelrath, A. T. Boothroyd, R. M. Ibberson, M. Brunelli, and S. J. Clarke, Structure and superconductivity of LiFeAs, Chem. Commun. **2008**, 5918 (2008).

[69] S. Graser, A. F. Kemper, T. A. Maier, H. P. Cheng, P. J. Hirschfeld, and D. J. Scalapino, Spin fluctuations and superconductivity in a three-dimensional tight-binding model for $BaFe_2As_2$, Phys. Rev. B **81**, 214503 (2010).

[70] N. Marzari and D. Vanderbilt, Maximally localized generalized Wannier functions for composite energy bands, Phys. Rev. B **56**, 12847 (1997).

[71] I. Souza, N. Marzari, and D. Vanderbilt, Maximally localized Wannier functions for entangled energy bands, Phys. Rev. B **65**, 035109 (2001).

[72] J. Kuneš, R. Arita, P. Wissgott, A. Toschi, H. Ikeda, and K. Held, Wien2wannier: From linearized augmented plane waves to maximally localized Wannier functions, Comput. Phys. Commun. **181**, 1888 (2010).

[73] A. A. Mostofi, J. R. Yates, Y.-S. Lee, I. Souza, D. Vanderbilt, and N. Marzar, Wannier90: A tool for obtaining maximally-localised Wannier functions, Comput. Phys. Commun. **178**, 685 (2008).

[74] S. Florens and A. Georges, Slave-rotor mean-field theories of strongly correlated systems and the Mott transition in finite dimensions, Phys. Rev. B **70**, 035114 (2004).

[75] M. Imada, A. Fujimori, and Y. Tokura, Metal-insulator transitions, Rev. Mod. Phys. **70**, 1039 (1998).